Origami-based cellular structures with in-situ transition between collapsible and load-bearing configurations

Hiromi Yasuda[1,2], Balakumaran Gopalarethinam[1], Takahiro Kunimine[3], Tomohiro Tachi[4], and Jinkyu Yang[1]

[1]Department of Aeronautics & Astronautics, University of Washington, Seattle, WA 98195-2400, USA
[2]Department of Mechanical Engineering and Applied Mechanics, University of Pennsylvania, Philadelphia, PA 19104, USA
[3]Faculty of Mechanical Engineering, Kanazawa University, Kakuma-machi, Kanazawa 920-1192, Japan
[4]Graduate School of Arts and Sciences, University of Tokyo, Tokyo 153-8902, Japan

March 18, 2019

Abstract

Periodic cellular structures are widely used for engineering applications due to their lightweight, space filling, and load supporting nature. However, the configuration of the cellular structures is generally fixed after they are initially built, and it is extremely difficult to change their structural properties – particularly their load bearing capabilities – in a controllable fashion. Here, we show that volumetric origami cells made of Tachi-Miura Polyhedron (TMP) can exhibit in-situ transition between flat-foldable and load-bearing states without modifying their predefined crease patterns or hitting the kinematically singular configuration. We theoretically study this mechanical bifurcation to establish our design principle, and verify this experimentally by fabricating self-folding TMP prototypes made of paper sheets and heat-shrinking films. We demonstrate the improvement of load carrying capabilities by 10^2 by switching the TMP from foldable to load-bearing configurations. These reprogrammable structures can provide practical solutions in various engineering applications, such as deployable space structures, portable architectures for disaster relief, reconfigurable packing materials, and medical devices like stents.

Introduction

Reconfigurable structures can transform their shapes without entailing the redesign of their achitectures[1],[2],[3],[4]. Recently, origami has gained increasing attention from the scientific and engineering community, because we can construct various types of reconfigurable cellular structures by simply folding surface materials. Examples include interleaved tube cellular structures[5], zipper-coupled tubes[6], waterbomb origami[7],[8] and prismatic architected materials based on snapology[9],[10]. These origami-based cellular structures exhibit great ability to transform their shape from one state to another. However, one of the major concerns of these structures is to solve the conflict between reconfigurable and load-bearing capabilities. Typically, reconfigurability needs structural flexibility, while load-bearing capability requires structural rigidity.

One way to achieve load-supporting property in origami is a self-blocking mechanism. For example, a stacked Miura-ori structure can significantly increase its maximum load capacity, once it reaches a densification

stage[11],[12]. This mechanism harnesses internal contact between layers, which constrains further deformation of the entire structure. While this mechanism brings a notable enhancement of structural stiffness in origami, such a structure inevitably hits the singular state (i.e., blocked state), from which its kinematic path becomes unpredictable. This makes the system impossible to be reconfigured back to the original state.

Previous studies have also reported non-locking mechanisms to achieve simultaneously reconfigurable and load-bearing capabilities[5],[6],[9] by constructing highly overconstrained mechanisms. However, it remains a formidable challenge to switch freely between the reconfigurable and load-bearing modes. Another approach shows the potential of programmable structures switching between different cross sections[13]. This method utilizes the kinematic bifurcation the singular state, leading to an exponential number of modes because of its combinational nature of the kinematics. The controlled actuation from such a kinematically singular state causes the uncertainty of the folding motion[14], making it theoretically impossible to switch reliably between modes.

Here, we show a new method of realizing a reliable switching between load-bearing capability and folding nature in origami-based cellular structures. Specifically, we exploit the mechanical bifurcation of the Tachi-Miura Polyhedron (TMP)[15],[16],[17], which exhibits the in-situ transition between two drastically different states: collapsible and load-bearing configurations (see Fig.1A for the conceptual illustration). This behavior is attributed to pure kinematic motions of the TMP cells, which possess a single folding path but with multiple local minima in its dimensions. Depending on the configuration of the TMP unit cell, the structure can be folded into the completely flat (see the schematic illustration marked by (i) in Fig.1B), or loading-carrying shape (see (ii) in Fig.1B, and the photograph for the corresponding paper prototype carrying approximately 17 times its own weight). It should be noted that this dual folding mechanism is based on a rigid origami motion, which means that all deformation takes place only along crease lines, without incurring elastic deformation or plastic buckling of planar facets. This is particularly important for engineering applications to construct a 3D architecture, because it would not necessitate curved or deformable facets. Moreover, the kinematic path depicted in the fold angle parameter space is regular between the states, meaning that the mechanism does not hit kinematic singularity and thus eliminating the uncertainty in the mode switch. Therefore, to actuate this structure, we only need to control the folding angle of the crease lines. To prove this concept, we analytically study the nonlinear kinematic behavior of TMP cells, fabricate paper-based TMP prototypes using a simple self-folding technique, and eventually demonstrate their self-folding actuation to trigger the in-situ transition between collapsible and load-carrying states.

Kinematics of the Tachi-Miura Polyhedron Unit Cell

The TMP unit cell is a bellows-like origami structure as shown in Figure 2a. The structure consists of two sheets (see Figure 2b for the crease patterns for the two sheets). Each sheet is composed of two symmetric layers (i.e., $N = 2$). The design of the TMP is defined by the three length parameters (l, m, and d as shown in Figure 2b) and the angle (α) between main (horizontal) and sub (inclined) crease lines. We can express the width (W) and breadth (B) of the cross-section of the TMP as follows [17]:

$$B = 2m \sin \theta_G + d \cos \theta_M \tag{1}$$
$$W = 2l + \frac{d}{\tan \alpha} + 2m \cos \theta_G, \tag{2}$$

where θ_M is a folding angle for the main crease lines (see the 3D view in Figure 2a), and θ_G is an angle which can be calculated from θ_M (see *SI Appendix*, section S1 for more details). Therefore, the posture of the TMP can be determined by only one folding angle (θ_M), implying its single degree-of-freedom (i.e., rigid foldable) nature.
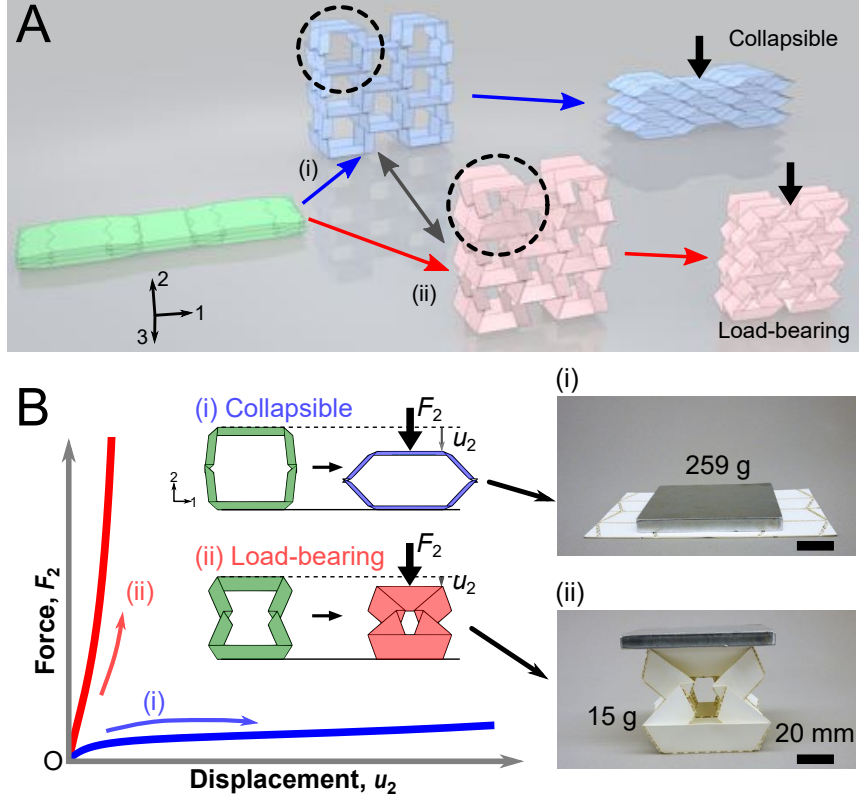
Figure 1: Conceptual illustration of the Tachi-Miura Polyhedron (TMP) cellular structure with tunable transition between collapsible and load-bearing states. a) The TMP structure can be folded into two distinctive configurations: (i) collapsible and (ii) load-bearing modes. The dashed circles indicate the single TMP cell with (i) convex and (ii) concave side postures. b) Illustration of the force-displacement relationship for the single TMP cell with those two configurations. The photographs shows the distinctive load-bearing capability of our paper-based TMP prototype between the two states.

We represent the folded state of the TMP by defining the folding ratio in terms of θ_M:

$$\gamma = \{\pi/2 \ - \theta_M\}/(\pi/2 \ ). \tag{3}$$

Based on this definition, at $\gamma = 0$, the unit cell is folded into the flat state in the 1-3 axes, whereas $\gamma = 1$ indicates the flat state in the 1-2 plane. Figure 2c shows the folding motion of two TMPs as a function of γ. Both have the same length parameters $(l, m, d) = (4, 4, 3)$, but possess different α values: 45° and 70°. For $\alpha = 45°$ case (the yellow colored TMP in Figure 2c), the cross-section retains the convex polygon as γ approaches 1. However, $\alpha = 70°$ case (the green colored TMP in Figure 2c) shows the transformation from the convex to the concave cross-sectional shape.

Now we investigate how the loading capabilities between the two configurations differ. To answer this question, we first analyze the breadth (B) change of the TMP unit cell as a function of γ for the two different α angles: 45 and 70 as shown in Figure 3a. Here, B is normalized by the value at $\gamma = 1$. The case of $\alpha = 45°$ shows that Bincreases monotonically as γ increases, and the structure takes its maximum value at $\gamma = 1$. On the other hand, the TMP with $\alpha = 70°$ exhibits the non-monotonic change of B, and it reaches the maximum breadth at the critical folding ratio, $\gamma_C = 0.28$.

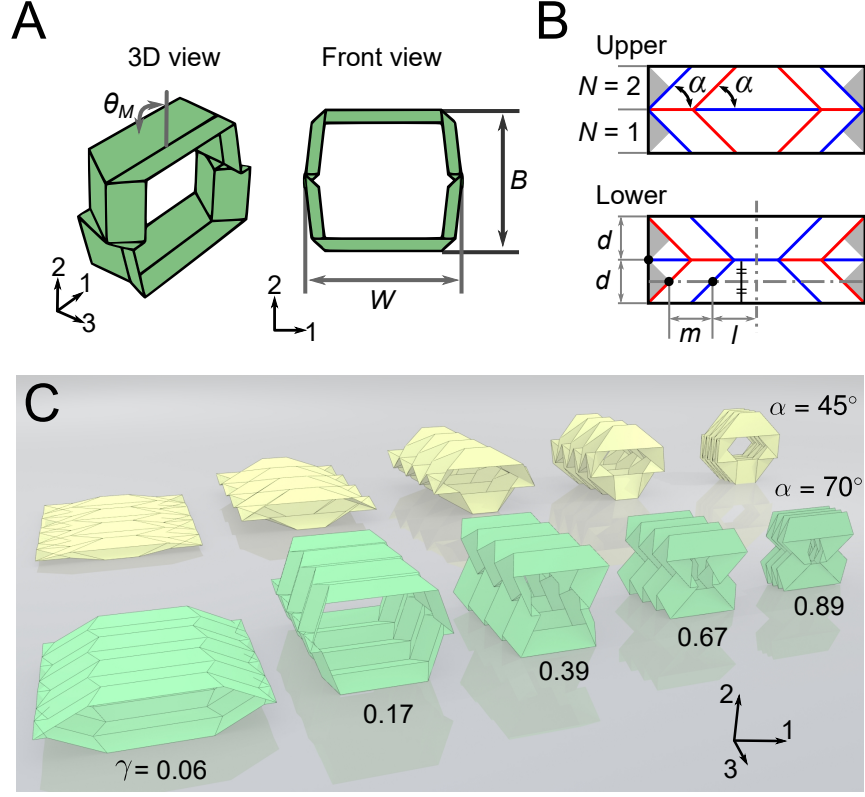It is this non-monotonic shape of B that endows both collapsible and load-bearing capabilities of the TMP.

3

Figure 2: Geometry of the TMP. (*A*) The TMP unit cell is shown in the 3D view (*Left*) and the front view (\textit{Right}). (*B*) The crease patterns of the TMP unit cells are described. The red and blue lines indicate the mountain and valley creases, respectively. The gray area is the adhesive region to connect these two sheets. (*C*) The TMP structure can be folded from the initial flat state to the other flat configuration (from left to right). The design parameters used are $(l, m, d) = (4, 4, 3)$, $N = 7$, and $\alpha = 45$ (yellow) / 70 (green).

That is, if we apply compression to the TMP along the 2-axis (i.e., decreasing B), the structure will collapse when the initial configuration of the TMP is positioned on the left side of the critical point (marked by (i) in Figure 3a). However, if the initial posture of the TMP is on the right side of the critical point (case (ii) in Figure 3a), the structure will deform in a way that its breadth is maintained kinematically, which leads to the load-bearing capability under assumption of rigid origami.

It is notable that the choice of this mechanical bifurcation between collapsible and load-bearing modes is determined by the initial posture of the TMP, without necessitating the manipulation of its crease patterns. We also observe from the inset illustrations in Figure 3a that the cross-section of the collapsible mode shows a convex shape, whereas the load-bearing configuration exhibits a concave shape. The close relationship between the TMP's auxetic and load-bearing properties is discussed in \textit{SI Appendix} (Fig. S2 and section S2 for more details).

The next question is naturally how we design the TMP unit cell to exhibit the bifurcated folding motion described above. This design problem requires studying the critical transition behavior of the TMP in various
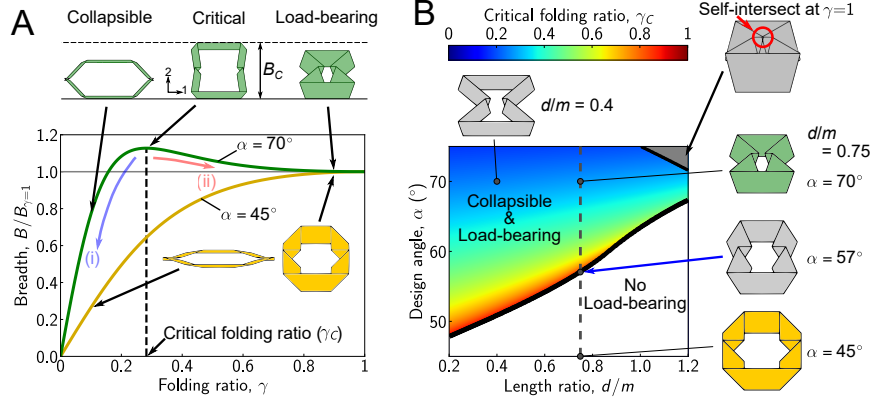
Figure 3: Kinematic analysis on the TMP unit cell. (*A*) The breadth (*B*) is examined as a function of the folding ratio (γ) for the two different α values: 45 (yellow) and 70 (green). The inset illustrates the cross-sectional geometry change for each folding stage. For $\alpha = 70$, the structure takes its maximum value of *B* at the critical folding ratio ($\gamma_C = 0.28$). (*B*) This critical folding ratio can be tuned by altering the length ratio (d/m) and crease angle (α). The lower black solid curve is the boundary between the configuration with/without the critical transition. The gray area indicates the invalid design parameters due to the self-intersection of TMP facets. The red arrow in the upper inset points to the collision between the side parts.

length ratios (d/m) and crease angles (α). For the sake of simplicity, we fix $l = m$. First, we check the existence of the critical folding angle (γ_C) by solving $dB/d\theta_M = 0$, which leads to

$$\cos \theta_G = \frac{1}{2} \left\{ -1 + \sqrt{1 - \frac{2\,(d/m\,)}{\tan \alpha}} \right\}. \tag{4}$$

From this θ_G, we obtain θ_M (*SI Appendix*, section S1) and, in turn, γ_C ((3)). If this process yields γ_C in the reasonable range (i.e., $0 < \gamma_C < 1$), the TMP design exhibits the mechanical bifurcation with a controllable load-carrying capability. Otherwise, it will show only collapsible motions under loading.

Based on Eq. 4, various configurations of the TMP are examined in the design space as shown in Figure 3b. Here, the color intensity represents the value of γ_C between 0 and 1, such that the colored area denotes the design space where the critical transition takes place during the folding motions of the TMP. The white area shows the design space with γ_C outside the reasonable range. In this case, the TMP will present only a collapsible folding motion, no matter where the initial posture is set. For example, if $d/m = 0.75$ is selected (dashed vertical line in Figure 3b), the TMP exhibits collapsible motions at $\alpha = 45°$, showing the convex cross-sectional shape during folding (see the inset for the cross-sectional shape at $\gamma = 1$). As we increase α, the TMP starts to change its cross-sectional shape from the convex to concave geometry. At $\alpha = 70°$, the TMP takes the concave cross-sectional shape, enabling both collapsible and load-bearing behavior. This finding is consistent with the folding and load-carrying motions of the TMP shown in Figures 2c and 3a.

The boundary between the colored and white zones can be calculated numerically by solving Eq. 4. The result is shown in the solid black curve in Figure 3b. In the case of $d/m = 0.75$, the boundary is formed at $\alpha = 57°$ (see the crossing between the black curve and the vertical dashed line in Figure 3*B*). Note in passing that if we consider an infinite chain of TMP unit cells stacked in the 2-axis, this boundary approaches $\alpha = 45°$ regardless of the length ratio (see *SI Appendix*, section S3 for more details). We also find that not all parameters considered in this design space produce a realistic TMP structure. In Figure 3b, the gray colored area represents a forbidden design space, where the collision between the side facets happens (see the upper right inset in Figure 3b). Mathematically, this self-intersection can be avoided if $2l - d\cot(\alpha) + 2m\cos(2\alpha) > 0$ [17], and this boundary (upper black curve) is shown in Figure 3b.

5

Experimental Verification of the Single TMP Analysis

Implementation of self-folding creases

To verify our design principle, we fabricate TMP prototypes made of paper sheets and conduct compression tests on single TMP unit cells. As we discussed in the previous section, the key point is to observe two highly distinctive folding motions: collapsible and load-bearing behavior below and above the critical folding ratio (γ_C), respectively. To fine tune the initial posture of TMP prototypes around this critical point, we introduce a simple self-folding mechanism based on heat-shrink Polyvinyl chloride (PVC) films. Figure 4a illustrates the layout of our self-folding hinge consisting of five layers, including the PVC film (see Materials and Methods, and also Movie S1). In this design, there is a gap (denoted by L_{gap} in Figure 4a) between the pairs of inserted layers (with arm length L_1). When the PVC film is heated by using a heat gun in this study, the contraction of the PVC film generates the bending moment, eventually closing this gap. Figure 4b shows the snapshots of the self-folding process, when $L_{gap} = 2$ mm and $L_1 = 18$ mm (Movie S1).
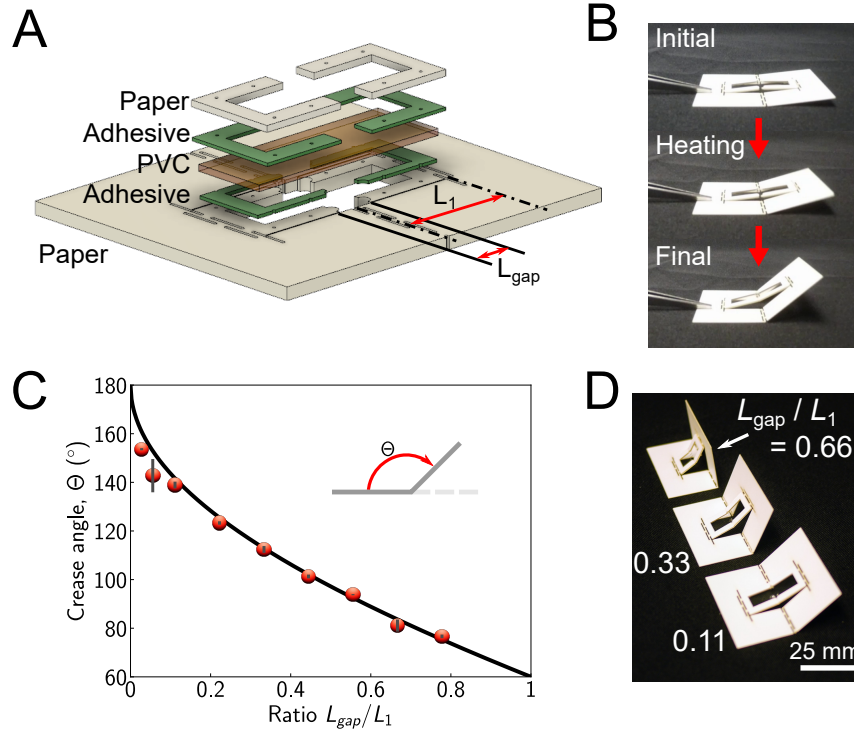

Figure 4: Design and verification of the self-folding crease. (A) The layout of the self-folding crease. (B) The self-folding process triggered by heat. (C) The self-folding process is characterized by the final crease angle (Θ) as a function of L_{gap}/L_1. (D) The photographs show three folded configurations controlled by L_{gap}/L_1. We use $L_1 = 18$ mm for all experimental prototypes.

In the self-folding process, the final folded crease angle (Θ as shown in the inset of Figure 4c) is governed by the ratio of L_{gap}/L_1. If we allow a smaller L_{gap}/L_1, the crease will be bent less (i.e., Θ closer to $180°$), whereas the larger L_{gap}/L_1 will induce a more drastic bending (i.e., smaller Θ). Figure 4c shows Θ as a function of L_{gap}/L_1 for various prototypes. Here, the red markers represent the experimental measurements from three prototypes per designated L_{gap}/L_1 value, and the black curve is the prediction from our geometrical model (see *SI Appendix*, section S4 for more details). Figure 4d shows the digital images of the three different crease angles achieved by imposing $L_{gap}/L_1 = 0.11, 0.33,$ and 0.66.

Compression tests on TMP unit cells

For the fabrication of the TMP cells, we choose their geometrical parameters of $(l, m, d) = (40, 40, 30)$ mm, $N = 4$, and $\alpha = 70°$, which result in $\gamma_C = 0.28$ according to the established design guideline (Figure 3b). Using these design parameters, we fabricate two types of the TMP prototypes with distinctive initial folded state (γ_0): one with $\gamma_0 < \gamma_C$ for the collapsible behavior, and the other with $\gamma_0 > \gamma_C$ for the load-bearing feature. We achieve the change of this initial folded state by leveraging the self-folding mechanism described in the previous section. Specifically, we manipulate L_{gap}/L_1 to obtain (i) $\gamma_0 = 0.21$ for collapsible behavior $(L_{gap}/L_1 = 0.11)$ and (ii) $\gamma_0 = 0.37$ for load-bearing feature $(L_{gap}/L_1 = 0.33)$. The positions of these initial folded states with respect to the critical point are shown in Figure 5a along with their cross-sectional geometries.
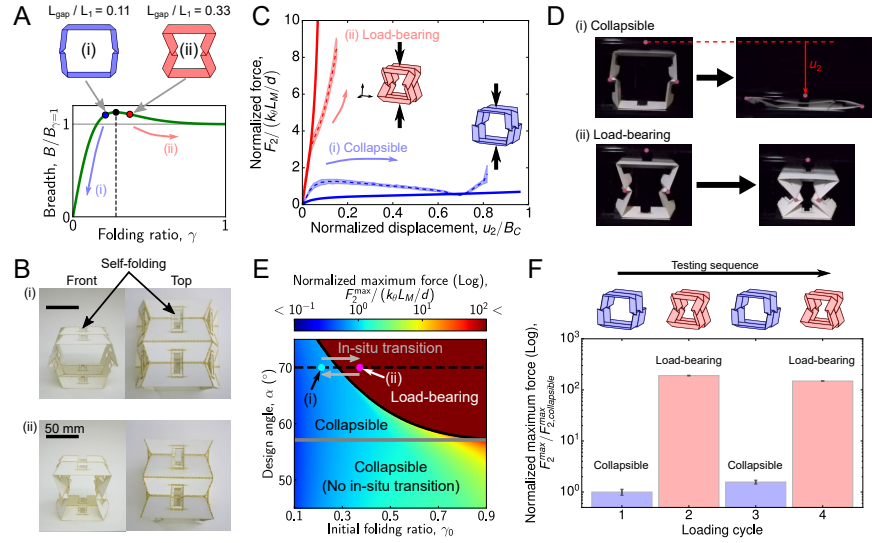

Figure 5: Experimental demonstration of the TMP unit cell with in-situ transition between collapsible and load-bearing states. a) View of the TMP with two different initial folded states: (i) collapsible ($\gamma_0 = 0.21$) and (ii) load-bearing configurations ($\gamma_0 = 0.37$). b) Digital images of (i) collapsible and (ii) load-bearing prototypes with the self-folding crease lines denoted by the arrows. c) Experimentally measured force-displacement curves (dashed curves with colored bands representing mean values with standard deviations) are compared with the analytical prediction from the rigid origami model (solid curves). d) The initial (*Left*) and final (*Right*) shapes of the cross-section under loading. e) The surface plot of the maximum force required to compress the TMP as a function of γ_0 and α. The markers denoted by the arrows (i) and (ii) correspond to the prototypes of the collapsible and load-bearing configurations, respectively. The gray horizontal line is at $\alpha = 57^{\circ}$, corresponding to the boundary between the configurations with/without load-bearing capability. % as denoted by the blue arrow in Fig.~**??**\textit{B}. (\textit{F}) Cyclic loading is applied to demonstrate the in-situ transition between the two configurations. The maximum force required to compress the TMP is measured, and is normalized by the force in the first cycle. The insets illustrate the target configurations.

We conduct compression tests on these two different prototypes. Figure 5c shows the force (F_2) and displacement (u_2) relationships for (i) the collapsible (blue) and (ii) load-bearing (red) configurations. Here, the dashed curves with bands represent the experimental measurements with standard deviations, and the solid curves show the analytical prediction based on the rigid origami model. In the analytical model, the crease lines in the TMP are modeled as a hinge with a torsion spring (see *SI Appendix*, section S5 for more

details). The spring constant k_θ is defined per unit length of the crease, and the value of this constant is obtained from the experiment on a single crease line (see *SI Appendix*, section S6 for more details). The force is normalized by k_θ, d, and the total length of the main crease line (L_M, see *SI Appendix* for details). Similarly, the displacement is non-dimensionalized by the maximum TMP height at the critical point (i.e., B_c as indicated in Figure 3a). In Figure 5c, we clearly observe two drastically different behaviors between the load-bearing and collapsible configurations. The experimental results corroborate our analytical prediction. In the load-bearing configuration, however, the deviation between the experimental and predicted results increases toward the end of compression. This is due to the limitation of our rigid origami model, in which we assume that all surfaces maintain their shapes without deformation during folding/unfolding motions. However, if the structure approaches $\gamma = 0$ or 1, the facet deformation is inevitable because of the effect of material thickness and the friction between the prototype and the stage of the testing setup (see Figure 5d, and Movie S3 and S4 for compression of the collapsible and load-bearing configuration). For the collapsible case, the initial increase of the force is greater than the prediction, and this is attributed to the resistance of PVC films in the process of unfolding. Despite the effect of the friction and surface deformation, the collapsible configuration needs much smaller force to be folded into a flat stage (i.e., $\gamma = 0$), compared to the maximum force sustained in the load-bearing stage (i.e., towards the direction of $\gamma = 1$). We further investigate the drastic contrast of the TMP's load-bearing capability in relation to design parameters and initial conditions. For this, we use the rigid origami model and examine how much force is required to compress the TMP to the completely collapsed or load-bearing configurations. In this analysis, if γ_0 is below (above) γ_C, we calculate the maximum force required for the folding between γ_0 and $\gamma = 0$ ($\gamma = 1$). Figure 5e shows the surface map of the maximum force required as a function of γ_0 and α in case $l/m = 1$ and $d/m = 0.75$. The black solid curve in this figure represents the boundary between the collapsible and load-bearing configurations, which is calculated from Eq. 4. The surface map clearly shows the two distinctive zones, representing collapsible and load-bearing configurations. The two fabricated prototypes are indicated by the circular markers, (i) and (ii), in Figure 5e. By crossing the boundary from (i) to (ii), the structure exhibits a significant increase of the maximum support force by orders of magnitude. Ideally the maximum force becomes an infinity in the load-bearing stage as the TMP approaches $\gamma = 1$. In experiments, however, the surface deformation and buckling take place before reaching such an extremely high force. Now we demonstrate the in-situ transition between the two modes in cycles and measure the contrast of the support force experimentally. We prepare TMP prototypes made of seven layers ($N = 7$) and remove the one-way, self-folding creases for the repeatable in-situ transition. We manually change their initial conditions between collapsible and load-bearing states and measure the force applied to the prototypes for each loading cycle (see Movie S5 for the in-situ transformation of the paper prototype used for this cyclic loading test). Figure 5f shows the experimental results with the insets illustrating the target configurations. Here, the measured force is normalized by the force required to compress the collapsible configuration ($\gamma_0 = 0.21$) to a flat stage in the first cycle. We observe drastic contrast of load-carrying capabilities between the two stages (blue and red for collapsible and load-carrying configurations). Quantitatively, even though the prototypes are made of paper sheets and are loaded up to the repeatable elastic regime, the TMP increases the maximum support force by two orders of magnitude, simply by changing the initial posture from the collapsible to the load-bearing state. This verifies the capability of the TMP to achieve both reconfigurable and load-carrying capabilities in a controllable manner.

Design/Fabrication of TMP-based Cellular Structures

Finally, we explore the design and fabrication of space filling tessellations by using the TMP cells as a building block (Figure 6a). Such a cellular structure derives its unique characteristics from the comprising TMP unit cells [15],[16],[17]. We fabricate a physical prototype consisting of eight TMP unit cells by employing the same design parameters used in the previous section (Figure 6b). We find the cellular assembly also shows the in-situ transition between collapsible and load-bearing behaviors (Movie S6). Based on this in-situ transition, one of the potential applications of the TMP cellular structure is a deployable bridge for disaster relief.

Figure 6c shows the conceptual illustration of the deployment of the TMP-based bridge-like structure, which can be folded flat for stowing and can be deployed for load carrying purposes (see Movie S7 for its deployment motion). Similarly, TMP architectures can be used for constructing a deployable–yet stiff–space structure for space habitats (see *SI Appendix*, Fig. S7). While this study focuses on paper-based TMP prototypes, the design principle can be applied to different fabrication materials and approaches. For example, we can construct a TMP structure made of rigid acrylic panels (see Fig. S8 for its geometrical configurations and Movie S8 for its folding motion). On the contrary, we can also fabricate soft TMP structures by using additive manufacturing techniques. We explore the feasibility by printing TMP-based soft cellular structures made of thermoplastic polyurethane elastomer (Fig. S9). Using this fabrication approach, we show that two seemingly identical TMP cells can present drastically different load-carrying behaviors (Movie S9). These additive manufacturing techniques can potentially enhance fabrication accuracy, ease manufacturing processes, and open new applications for TMP structures.
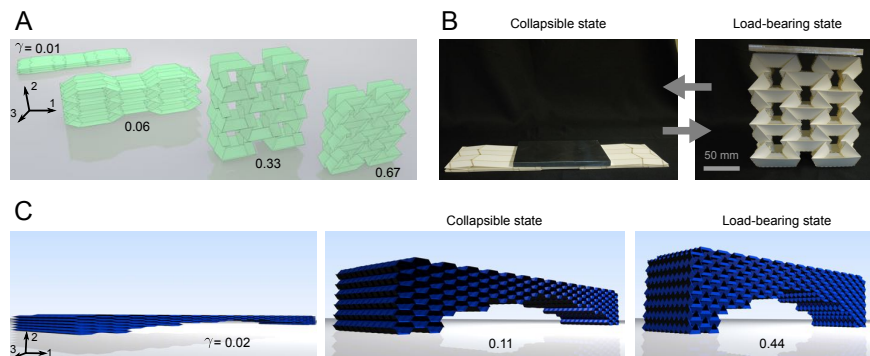

Figure 6: Tessellations of the TMP unit cell. (*A*) Folding motion of the TMP cellular structure is shown. (*B*) The cellular structure composed of eight TMP unit cells exhibits in-situ transition between collapsible (*Left*) and load-bearing (*Right*) configurations. (*C*) Conceptual illustration of a deployable TMP-based bridge with the simultaneously deployable and load-bearing capability.

Conclusions

We have analyzed and demonstrated highly versatile folding behavior of the Tachi-Miura Polyhedron (TMP) by employing rigid origami model and paper-based prototypes with self-folding creases. We showed that this volumetric origami can exhibit two drastically different configurations, collapsible and load-bearing ones, without modifying the predefined crease patterns. This is achieved by leveraging a mechanical bifurcation intrinsic in TMP, which enables in-situ transition between the collapsible and load-bearing states in an efficient and controllable manner. For experimental demonstrations, we employed a self-folding technique based on heat-shrinking films. Although this mechanism supports the one-way actuation only, we envision that the TMP cellular structures can also transform their shapes repeatedly by using two-way reversible actuation methods such as shape memory alloys and electroactive polymer actuators. This is possible because the kinematic nature of TMP allows the switching without hitting a singular state. While the contrast of load-carrying capabilities between compliant and sturdy modes was in the range of 10^2 for the paper model, we expect the contrast would vary depending on the types of materials, such as acrylic and 3D printed TMP architectures demonstrated in this study. We envision that the TMP architectures can be employed to a wide range of engineering applications, such as a portable bridge for disaster relief, deployable space habitat, and medical devices.

Supporting Information

Supporting Information is available from the Wiley Online Library or from the author.

Acknowledgements

Keyword

Rigid origami, load-bearing capability, self-folding

References

[1]M. Yim, W.-min Shen, B. Salemi, D. Rus, M. Moll, H. Lipson, E. Klavins, G. Chirikjian, *IEEE Robotics & Automation Magazine* **2007**, *14*, 43.

[2]E. Hawkes, B. An, N. M. Benbernou, H. Tanaka, S. Kim, E. D. Demaine, D. Rus, R. J. Wood, *Proceedings of the National Academy of Sciences* **2010**, *107*, 12441.

[3]B. Haghpanah, L. Salari-Sharif, P. Pourrajab, J. Hopkins, L. Valdevit, *Advanced Materials* **2016**, *28*, 7915.

[4]D. Z. Rocklin, S. Zhou, K. Sun, X. Mao, *Nature Communications* **2017**, *8*, 14201.

[5]K. C. Cheung, T. Tachi, S. Calisch, K. Miura, *Smart Materials and Structures* **2014**, *23*, 094012.

[6]E. T. Filipov, T. Tachi, G. H. Paulino, *Proceedings of the National Academy of Sciences* **2015**, *112*, 12321.

[7]B. H. Hanna, J. M. Lund, R. J. Lang, S. P. Magleby, L. L. Howell, *Smart Materials and Structures* **2014**, *23*, 094009.

[8]Y. Chen, H. Feng, J. Ma, R. Peng, Z. You, *Proceedings of the Royal Society A: Mathematical Physical and Engineering Science* **2016**, *472*, 20150846.

[9]J. T. B. Overvelde, T. A. de Jong, Y. Shevchenko, S. A. Becerra, G. M. Whitesides, J. C. Weaver, C. Hoberman, K. Bertoldi, *Nature Communications* **2016**, *7*, 10929.

[10]J. T. B. Overvelde, J. C. Weaver, C. Hoberman, K. Bertoldi, *Nature* **2017**, *541*, 347.

[11]M. Schenk, S. D. Guest, *Proceedings of the National Academy of Sciences* **2013**, *110*, 3276.

[12]H. Fang, S.-C. A. Chu, Y. Xia, K.-W. Wang, *Advanced Materials* **2018**, *30*, 1706311.

[13]E. T. Filipov, G. H. Paulino, T. Tachi, *Proceedings of the Royal Society A: Mathematical Physical and Engineering Science* **2016**, *472*, 20150607.

[14]T. Tachi, T. C. Hull, *Journal of Mechanisms and Robotics* **2017**, *9*, 021008.

[15]K. Miura, T. Tachi, *Journal of the International Society for the Interdisciplinary Study of Symmetry* **2010**, *9*, 204.

[16]T. Tachi, K. Miura, *Journal of the International Association for Shell and Spatial Structures* **2012**, *53*, 217.

[17]H. Yasuda, J. Yang, *Physical Review Letters* **2015**, *114*, 185502.